JAAS

PAPER

View Article Online
View Journal | View Issue

Cite this: *J. Anal. At. Spectrom.*, 2024, **39**, 3151

Automated detection of element-specific features in LIBS spectra

Zuzana Gajarska, *[a] Anna Faruzelová, [b] Erik Képeš, [bc] David Prochazka, [bc] Pavel Pořízka, [bc] Jozef Kaiser, [bc] Hans Lohninger [a] and Andreas Limbeck [a]

This work introduces a novel semi-automatic approach to identify elemental lines in spectra obtained *via* laser-induced breakdown spectroscopy (LIBS). The algorithm is based on unique spectral fingerprints of individual elements that are configured into comb-like filters. The element-specific filters are then correlated with measured spectra for semi-supervised qualitative analysis of samples. Spectral variations are accommodated by adjusting the micro-parameters of the comb filter. This step ensures accurate results despite minor deviations from the instrument's ideal calibration due to instrumental fluctuations, *e.g.*, drift in spectral calibration or line broadening. Additionally, the algorithm can autonomously detect spectral interference regions, aiding the analyst in verifying spectral lines where such interference may occur. The paper presents a comprehensive overview of the algorithm and discusses the main concepts, parameters, optimization steps, and limitations using Echelle spectra of two standard reference materials with different complexity: borosilicate glass (NIST 1411) and low-alloyed steel (SUS1R). Furthermore, the transferability of the approach to different scenarios and real-life applications is demonstrated using a single-channel Czerny–Turner spectrum of an amalgam filling extracted from a hyperspectral image of a human tooth. A demo of the algorithm is publicly available for non-commercial purposes.

Received 4th July 2024
Accepted 15th October 2024

DOI: 10.1039/d4ja00247d

rsc.li/jaas

1 Introduction

Laser-induced breakdown spectroscopy (LIBS) has become a promising tool for rapid elemental mapping of complex sample matrices[1] in diverse application fields, including biomedicine,[2–5] geology,[5–7] material analysis,[8] plant analysis[9,10] and exploration of space.[11–13] Although several efforts have been made to interpret LIBS spectra automatically,[14–17] the development of a universal tool for the automated detection of element-specific features in LIBS spectra proved to be a great challenge. The main reason is the inherent complexity and high variability of the spectra arising from different sample matrices and experimental conditions.[18]

To this day, the interpretation of LIBS spectra heavily relies on the manual identification and pre-selection of the most prominent lines by LIBS practitioners.[18,19] Considering the volume and the complexity of LIBS data obtained from imaging instruments, this process is not only time-consuming but also challenging, especially for complex or unknown samples. In such scenarios, even the most experienced users often resort to tedious database searches to identify the lines suitable for the analysis.

While deep learning methods hold a great promise to the field,[20] they are far from being integrated in the daily evaluation routines of LIBS practitioners. Additionally, in high-stakes applications such as cancer detection, where the accuracy and reliability of the models might have a profound effect on human life, it is still preferable to select the input features based on domain expertise.

To address this issue and facilitate the process, we developed an intuitive, user-friendly tool for the allocation and visualization of element-specific features in LIBS spectra. The allocation is based on correlating so called "combs" (Fig. 1) with the spectrum. As discussed in the paper, considering entire fingerprints rather than single lines does not only allow for a more reliable allocation of the features, but also provides deep insight into spectral interference, a common struggle in the community.

This work provides a comprehensive overview of the pipeline, discussing the main concepts, parameters, optimization steps, and limitations on Echelle spectra of two standard reference materials with different complexity: borosilicate glass (NIST 1411) and low-alloyed steel (SUS1R). Additionally, the practical application and transferability of the developed approach are demonstrated on a single-channel Czerny–Turner spectrum of amalgam filling extracted from a hyperspectral image of a human tooth.

[a]*Institute of Chemical Technologies and Analytics, TU Wien, Getreidemarkt 9, 1060 Vienna, Austria. E-mail: zuzana.gajarska@tuwien.ac.at; hans@epina.at*
[b]*CEITEC Brno University of Technology, Purkyňova 656/123, 61200 Brno, Czech Republic*
[c]*Faculty of Mechanical Engineering, Brno University of Technology, Technická 2896/2, 61669 Brno, Czech Republic*

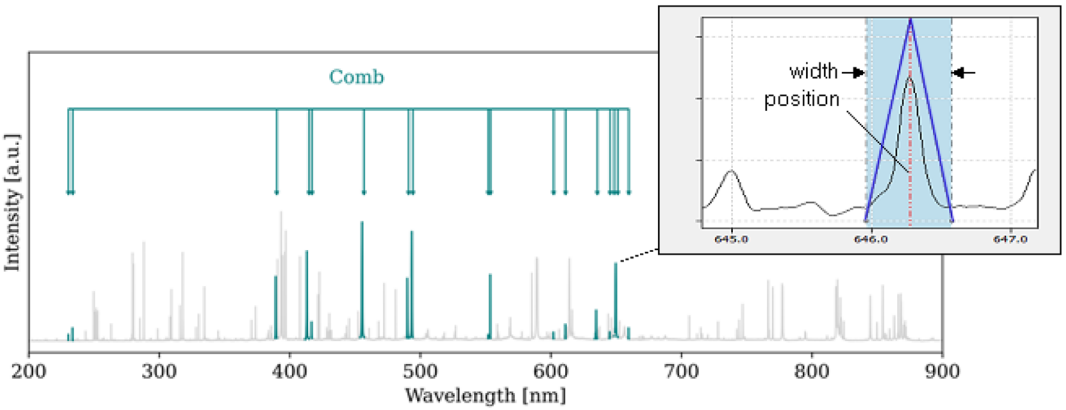

Fig. 1 Comb: a collection of triangular templates approximating Voigt profiles of the emission lines of an element. The small arrows indicate the positions of the templates. The breakout image indicates a single comb tooth (blue line) which can be adjusted in its position and width.

2 Materials and methods

2.1 Data acquisition

2.1.1 Standard reference materials (Echelle). The algorithm was developed using a LIBS dataset of two standard reference materials: borosilicate glass (NIST 1411 (National Institute of Standards and Technology, USA))[21] and low alloyed steel (SUS-1R (Federal Institute for Materials Research and Testing, Germany)).[22] All spectra were acquired with a LIBS Firefly instrument (Lightigo, Czech Republic) utilizing a pulsed Nd:YAG laser (20 Hz, 532 nm, 10 ns), an echelle spectrometer, and an electron multiplying charge-coupled device (EMCCD). The acquired spectral range was 200 to 1500 nm. The resolving power ($\lambda/\Delta\lambda$) of the instrument was 5000. Each sample was analyzed using a spot size of 100 μm, 10 accumulations, and 100 positions. The measurement was conducted under air (10 l min^{-1}) with distinct experimental conditions involving gradual changes in laser energy (from 5 to 140 mJ) and gate delay (from 100 ns to 20 μs). For further details on the experimental setup, we direct readers to the original publication.[23]

2.1.2 HSI of a human tooth (single-channel Czerny–Turner). The sample of the human tooth was extracted at the Faculty Hospital Ostrava regarding all the ethical requirements. The hyperspectral image was obtained using a FireFly LIBS system (Lightigo, Czech Republic) equipped with a Q-switched Nd:YAG ablation laser (266 nm, 50 Hz, 6 ns, 4 mJ). A single-channel Czerny–Turner spectrometer with an embedded CMOS detector was used to capture spectra in the range from 240 to 410 nm. During the measurements, an argon purge at a flow rate of 9 l min^{-1} was employed along with the extraction to prevent the redeposition of ablated material and potential cross-contamination of the biological and amalgam matrix. The surface of the sample was mapped with a spatial resolution of 20 μm in both axes, resulting in a map raster of 1235 × 835, with a total of 1 031 225 acquired spectra and an approximate analysis time of 5.7 hours.

All experiments were performed in accordance with the Guidelines of the Helsinki Declaration and approved by the ethics committee of the University Hospital of Saint Anne, Brno, Czech Republic (No. 01G/2020). Informed consents were obtained from all human participants in this study.

2.2 Comb algorithm

The comb algorithm is based on correlating combs (Fig. 1) with the spectrum. Each comb consists of a series of triangular shapes (the comb teeth) approximating Voigt profiles which are finally correlated with the spectrum.

Given the goal of universal applicability, the processing pipeline (Fig. 2) involves a series of intuitive steps designed to dynamically adjust to any possible variation in the baseline, presence, and characteristics of the emission lines. In the following, we describe the particular steps of the algorithm.

2.2.1 Line allocation. In the first step, the algorithm selects the corresponding range of the database and allocates the

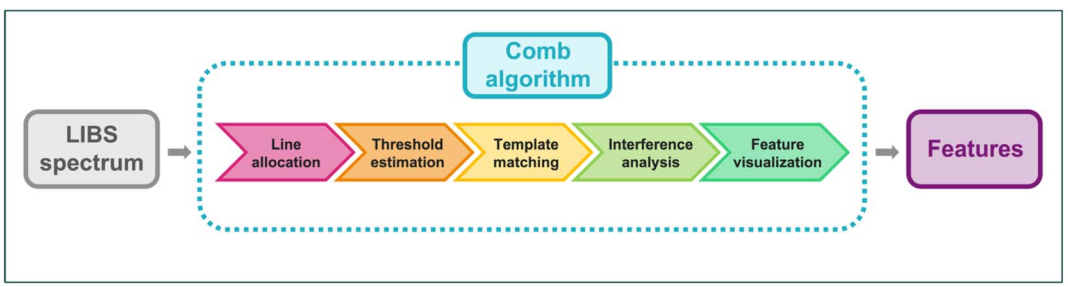

Fig. 2 Processing pipeline of the comb algorithm.

theoretical lines of each element to their positions. While ideally, a NIST database[24] (177 000 lines between 200 and 1000 nm, source: https://www.nist.gov/pml/atomic-spectra-database) would be employed, and the characteristics of the plasma and emitting species would be considered to update the list of relevant lines; for the development, we approximated this process by employing a limited database of the most prominent LIBS lines (1906 lines, source: Epina ImageLab, https://www.imagelab.at/; the database is available for download from Zenodo[25]).

2.2.2 Threshold estimation. To determine which of the theoretical lines might be present in the spectrum, the tool allows for setting a signal-to-noise (S/N) threshold based on the moving median and the percentile of the signal-baseline deviation. While any other baseline-estimation method could be used,[26] the moving median employs only a single intuitive parameter (the width of the moving window over which a median of the signal is calculated). This allows for robust baseline estimates while adapting well to new spectral scenarios. Following this process, the algorithm evaluates the deviation of the signal intensity from the baseline. As the significance of the information contained in a particular line is related to this deviation, we use a tunable upper percentile to provide a flexible S/N threshold following the trend of the baseline while surpassing the noise-related deviations.

2.2.3 Template matching. The presence of the allocated lines can be further supported by "matching" a comb (Fig. 1) at their assumed positions. The line is considered active if the intensity surpasses the S/N threshold, and the correlation between the signal intensity and the triangular template exceeds a threshold (0.5 by default). The total correlation of a fingerprint is calculated by evaluating the mean across all its active lines. Being independent of the line intensity, the correlation approach succeeds to detect all the lines exceeding the previously established S/N threshold, whether arising from major or trace constituents of the sample. Additionally, by evaluating the alignment of the theoretical and allocated line, the correlation provides insights into the possible shift and width of the lines.

As these parameters are not known *a priori*, the templates are initiated at default positions: line shift of 0.00 nm (assuming no shift relative to theory) and width of 1.00 nm (providing a broadening buffer). Subsequently, a comb of a single (reference) element is slightly moved in both directions (5 datapoints on each side) and the shift maximizing the correlation is retained. This way, the algorithm accounts for a uniform shift (*e.g.* instrumental shift) of all emission lines. As other shift sources (*e.g.* Stark shift) are difficult to estimate, they are not automatically accounted for. Nevertheless, by investigating the deviation of the allocated templates from the theoretical positions, the analysts can gain first insight into their presence.

To account for the line broadening, the templates of each fingerprint are gradually widened between the minimal possible template (3 datapoints) and user-defined maximum. The width maximizing the correlation is retained to approximate the regions where the lines reside. This accounts only for an element-specific broadening (*e.g.* Doppler broadening). Nevertheless, the broadening due to other effects (*e.g.* collisional/pressure broadening related to the population size and properties of the emitting species)[27–29] is not accounted for and can be further studied by investigating the deviation of the peak from the allocated template. All in all, after this step, the practitioners gain greater insight into the presence, position, shift and width of the emission lines of each element.

2.2.4 Interference analysis. Nevertheless, even after the allocation, it is not guaranteed that all the active fingerprint lines belong to the element of interest. To investigate the possible interference, the tool allows users to list all active lines in the region and visualize the corresponding fingerprints. To avoid possible artifacts and/or loss of information, the interferences are not resolved automatically. Nevertheless, the users have the possibility of manually deactivating less probable lines or entire element fingerprints, thereby excluding them from further analysis.

2.2.5 Feature visualization. In the final step, the users can visually explore fingerprints of either selected elements or top database hits. By offering a comprehensive overview of the active fingerprint lines, line correlations and possible interference, the interactive visualization provides an invaluable insight into the spectrum, providing analysts with numerous possibilities for subsequent data evaluation while facilitating informed decision-making.

3 Results and discussion

3.1 Standard reference materials

For a detailed discussion of the pipeline, we present spectra of two standard reference materials with different complexity: borosilicate glass (NIST 1411) and low-alloyed steel (SUS1R). The spectrum of the borosilicate glass exhibited low background emission and intense lines attributed to the high abundance of easily excitable elements (Table 1). The spectrum of low-alloyed steel featured complex baseline and high density of lines arising from the rich variety of transition elements present in the sample (Table 2). The following discussion is based on static representations of the two pipelines (Fig. 3 and 4). As the static figures cannot fully reflect the details/value of the features provided, the readers are highly advised to follow the discussion using the interactive demonstrations available at libsfeatex_demo_NIST1411 (https://colab.research.google.com/drive/1qmlSMMNvt5_ZczR6bYlUr5KvTUiZVaQV) (ref. 31) and libsfeatex_demo_SUS1R (https://colab.research.google.com/drive/1G-UAWBh-ZBpL-ZtmyxfY6lddqsXRIzx).[32]

3.1.1 Borosilicate glass (NIST 1411): case of a sparse spectrum. As presented in the Fig. 3a, the spectrum of borosilicate glass exhibited low background emission and intense lines of easily excitable elements (*e.g.* Na, Ca). To gain an informed insight into the spectrum, users can visualize fingerprints of different elements. In this case, we use the example of Ba, as it is present in the sample, provides multiple emission lines across the spectral range, and is less prominent than Na or Ca.

By examining the Ba lines (Fig. 3b), it becomes evident that the number of theoretical lines is relatively low due to the limited database used in the current work. While acceptable for

Table 1 NIST 1411: major element constituents of borosilicate glass[30]

Element	Concentration (ppm)	Selection of detected emission lines[a]
Si	271 337	Si I 251.61 nm, Si I 251.92 nm, Si I 252.41 nm, Si I 263.13 nm, Si I 288.17 nm, Si I 390.55 nm
Na	75 219	Na I 330.24 nm, Na I 330.3 nm, Na I 589.59 nm, Na I 818.33 nm, Na I 819.48 nm
Ba	44 780	Ba I 553.55 nm, Ba I 611.08 nm, Ba II 413.07 nm, Ba II 416.6 nm, Ba II 455.39 nm, Ba II 493.41 nm
B	33 980	B I 249.68 nm, B I 249.77 nm, B II 345.10 nm
Zn	30 931	Zn I 328.23 nm, Zn I 330.25 nm, Zn I 334.50, Zn I 468.01, Zn I 472.22 nm, Zn I 481.06 nm
Al	30 064	Al I 257.54 nm, Al I 308.21 nm, Al I 309.27 nm, Al I 394.41 nm, Al I 396.15 nm
K	24 654	K II 659.5, K I 766.49, K I 769.89
Ca	15 580	Ca I 422.67 nm, Ca I 430.25 nm, Ca I 430.77, Ca I 431.86, Ca I 442.54, Ca I 443.5 nm, Ca I 445.48 nm, Ca I 558.88 nm, Ca I 643.91 nm, Ca I 646.26 nm, Ca II 315.92 nm, Ca II 317.96 nm, Ca II 370.6 nm, Ca II 373.73 nm, Ca II 393.37 nm
Mg	1990	Mg I 383.20 nm, Mg I 383.79 nm, Mg I 383.83 nm, Mg I 389.19 nm, Mg I 518.37 nm, Mg II 279.09 nm, Mg II 279.55 nm, Mg II 279.81 nm, Mg II 280.27 nm
Sr	761	Sr I 460.73 nm, Sr I 472.23 nm, Sr II 407.78 nm, Sr II 421.55 nm, Sr II 430.54 nm
Fe	350	Fe I 373.49 nm, Fe I 373.71 nm, Fe I 404.58 nm, Fe II 259.94 nm, Fe II 263.13 nm
Ti	120	Ti II 323.45, Ti II 334.19, Ti II 334.94, Ti II 336.12

[a] A comprehensive overview of the available and detected emission lines can be found in the ESI file "lines_NIST1411.xlsx".

the development, this limitation shall be addressed by using a NIST database and employing an automated approach for filtering lines according to the conditions in the plasma.

To determine which of the theoretical lines might be present, we estimated a S/N threshold by defining the window size and percentile of baseline deviation. The window size regulates the extent of adjustment to the baseline variations. The percentile determines the horizontal location of the threshold, thus influencing the sensitivity of detection. In this case, a moving median with a window size of 10 nm and the 85-percentile resulted in a flexible threshold allowing for a good discrimination between the noise and the signal (Fig. 3c).

The threshold was exceeded at all theoretical locations of the lines, indicating their presence. Nevertheless, to further support this assumption, the regions of the spectra were correlated with triangular templates. As the exact shift and width of the lines were unknown, the templates were initiated at the theoretical positions (line shift of 0.00 nm, assuming no deviation from the database; and width of 1 nm, accounting for line broadening).

As shown by Fig. 3d, the centers of the templates seemed to align well with the lines, suggesting no systematic shift. Nevertheless, the templates were too wide, lowering the fingerprint correlation. This effect was not as pronounced in the regions with no interference (Fig. 3d, right). However, in the denser regions of the spectrum, the interfering/surrounding lines were included in the correlated regions, rendering the correlation low and the lines inactive (Fig. 3d, left). Thus, the templates were further refined utilizing the concept of the comb.

To investigate the assumption of no systematic shift, the comb of Ba (providing sufficient number of lines for a reliable estimate) was automatically shifted in both directions and the correlation tracked. As the average maximum was registered at a shift of 0.00 nm, the assumption was considered valid, and the fingerprint locations retained. To refine the width, the templates of each fingerprint were gradually adjusted, and the width maximizing the correlation retained. As shown in Fig. 3e, even though some of the lines were significantly wider than the template, the triangular shape of their tops resulted in high correlation, allowing their detection. Thus, while not providing a perfect fit, the simplification resulted in fast refinement and detection of the fingerprint lines, aligning well with the current goal.

Overall, all theoretical lines except two – Ba I 645.09 nm and Ba I 649.88 nm – were assessed by the algorithm as being active. Upon closer analysis of the comb and respective spectrum, this conclusion made by the algorithm seemed reasonable. The theoretical region of Ba I 649.88 nm was predominantly occupied by an intense line of Ba II 649.69 nm; and the only line present in the region of Ba I 645.09 nm was shifted to the left from the theoretical location. Upon hovering over the line, the algorithm identified Ca I 644.98 nm as the most likely alternative. To provide a more detailed comparison of the two alternatives, the fingerprints of Ca and Ba were rendered in an

Table 2 SUS-1R: major element constituents of low alloyed steel (excluding Fe)[22]

Element	Concentration (ppm)	Selection of detected emission lines[a]
Ni	29 000	Ni I 338.06 nm, Ni I 341.48 nm, Ni I 344.63 nm, Ni I 346.16 nm, Ni I 349.30 nm, Ni I 351.50 nm, Ni I 352.44 nm
Cr	17 000	Cr I 267.70 nm, Cr I 357.87 nm, Cr I 360.53 nm, Cr I 427.48 nm, Cr I 520.45 nm, Cr II 276.65 nm, Cr II 283.56 nm, Cr II 284.98 nm, Cr II 286.51 nm, Cr II 286.67 nm, Cr II 311.86 nm, Cr II 312.04 nm
Mn	11 000	Mn I 279.48 nm, Mn I 279.83 nm, Mn I 380.67 nm, Mn I 403.06 nm, Mn I 403.31 nm, Mn I 403.45 nm, Mn I 475.4 nm, Mn I 478.34 nm, Mn II 257.61 nm, Mn II 259.37 nm, Mn II 260.57 nm, Mn II 262.56 nm, Mn II 293.31 nm, Mn II 293.93 nm, Mn II 294.90 nm
C	9000	C II 588.98
Mo	9000	Mo I 317.03 nm, Mo I 379.83 nm, Mo I 550.60 nm, Mo II 292.34 nm, Mo II 329.23 nm
Si	8000	Si I 263.13 nm, Si I 288.17 nm
P	200	P I 253.57 nm
S	170	—
Cu	140	Cu I 276.64 nm, Cu I 324.74 nm, Cu I 327.40 nm, Cu I 510.53 nm
Nb	105	Nb I 405.89 nm, Nb II 294.15 nm, Nb II 309.42 nm, Nb II 313.08 nm, Nb II 318.03 nm, Nb II 321.56 nm, Nb II 322.55 nm, Nb II 325.41 nm
V	59	V II 290.88, V II 318.85
Co	21	Co I 350.23 nm, Co I 350.63 nm, Co I 351.03 nm
W	3	W II 259.87 nm (false positive)

[a] A comprehensive overview of the available and detected emission lines can be found in the ESI file "lines_SUS1R.xlsx".

interactive visualization (Fig. 3f). Displaying only the active lines of both fingerprints, the visualization clearly resolved the issue, providing further support for the presence of Ca I 644.98 nm.

For a more comprehensive overview of the sample contents, the users can visualize fingerprints of selected elements or top database hits (*e.g.*, fingerprints having the greatest number of active lines or fractions of active lines, *etc.*). As shown in Fig. 3g, in this case, the top 7 hits (Na, Si, Al, Ba, Zn, Ca and Sr) aligned relatively well with the contents of the sample (Table 1).

3.1.2 Low alloyed steel (SUS1R): case of an overpopulated spectrum. Compared to the spectrum of the borosilicate glass (NIST 1411), the spectrum of low-alloyed steel (SUS1R; Fig. 4a) exhibited a more complex baseline and higher density of lines arising from a variety of transition elements present in the sample (Table 2). This time, we demonstrate the fingerprint of chromium (Cr) to discuss the algorithm's ability to detect trace constituents within an iron-rich matrix and the current limitations related to the detection of Stark-shifted lines.

The listing of the theoretical lines (Fig. 4b) shows which Cr lines are available and considered for the analysis. As before, the number of available lines was relatively low, hinting at the limited database employed during the development.

The intuitive and easily adjustable parameters of the S/N threshold proved to be of great value, especially when dealing with such a complex spectrum of low-alloyed steel. In this case, we employed a slightly narrower window size (8 nm) to accommodate the more dynamic variations of the baseline and a higher baseline-deviation percentile (90) to account for the increased noise fluctuations. This enabled to establish a flexible threshold adjusting well to the fluctuations of the baseline, while surpassing the deviations of the noise (Fig. 4c). As the figure shows, most of the theoretical lines appeared above the threshold.

To further support their presence, the respective regions were correlated with triangular templates. As no *a priori* information about the shifts and widths of the lines was available, the templates were first correlated at the assumed/theoretical positions (line shift of 0.00 nm, width of 1.0 nm). As depicted in the Fig. 4d, the allocation of the templates in the spectrum hinted at no systematic shift. Nevertheless, as in the case of NIST 1411, the default templates were too wide, rendering the correlation below the threshold of 0.5, leaving some lines undetected. As discussed before, especially in such densely populated areas, the width of the templates becomes critical, as the regions include parts of other lines. Thus, the correlated shapes no longer match, the correlation falls below the threshold and the lines become undetected.

To validate the assumption of no systematic shift and assure the fingerprint locations, the fingerprint of Fe (the major component of the sample with the most active lines) was

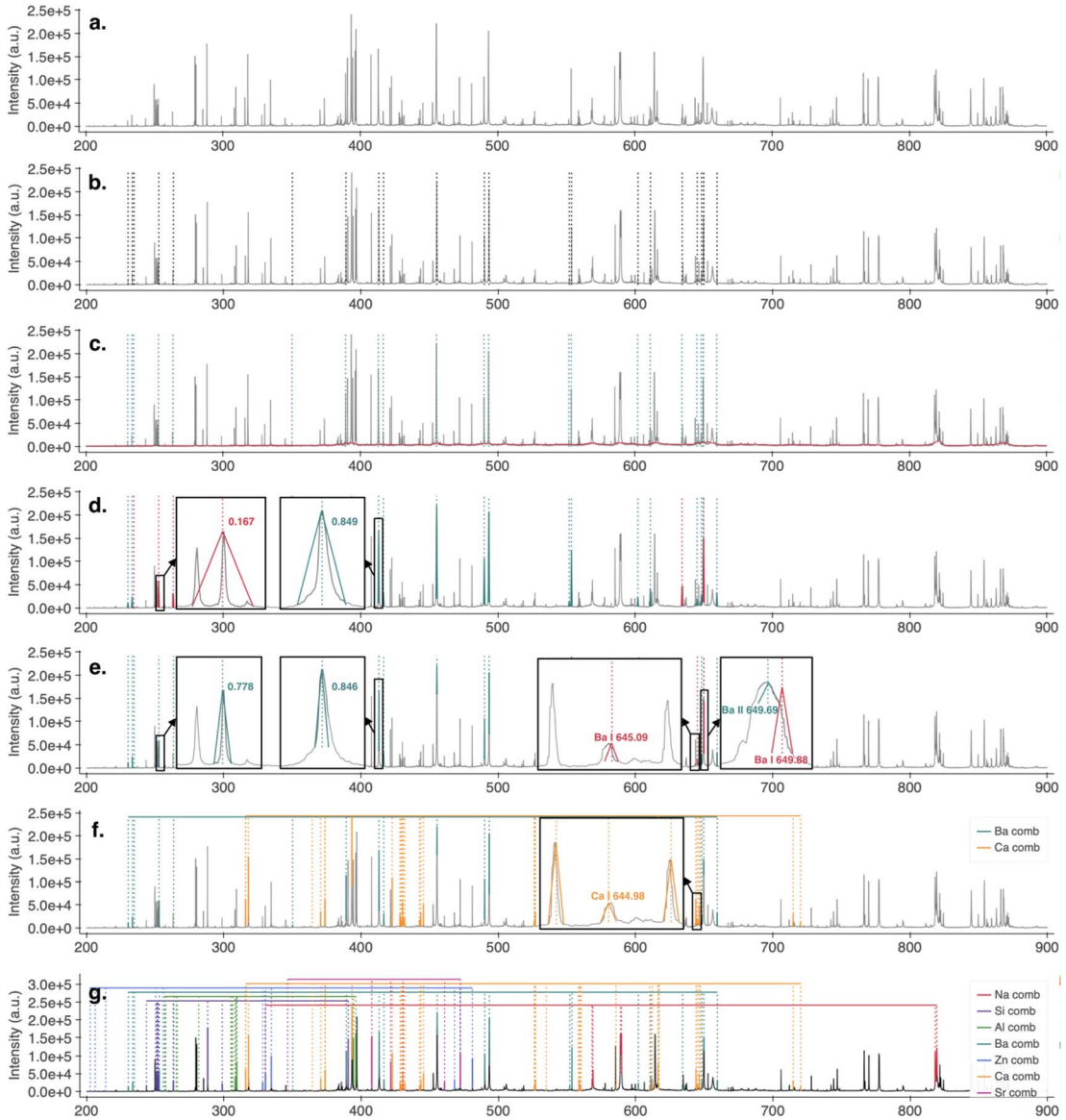

Fig. 3 Comb pipeline of borosilicate glass (NIST1411), laser energy 140 mJ, gate delay 1400 ns: (a) LIBS spectrum; (b) line allocation: theoretical lines of Ba; (c) threshold estimation: above-threshold lines of Ba; (d) template matching: default templates of Ba (shift 0.00 nm, width 1.00 nm, correlation active lines: 0.59); (e) template matching: optimized templates of Ba (shift 0.00 nm, width 0.26 nm, correlation active lines: 0.84); (f) interference analysis: combs of Ba and Ca; (g) feature visualization: elemental fingerprints of the top 7 hits.

slightly shifted and the correlation tracked. Since the average optimum of lines lay at a shift of 0.00 nm, the positions of the fingerprints were retained. To refine the excess width, the templates were gradually adjusted until maximum correlation was achieved.

Despite these adjustments, the number of detected lines remained relatively low (Fig. 4e). A closer look at the corresponding regions revealed several issues. First, the line of Cr II 284.32 nm was located in the theoretical region, but an interference from a neighboring line resulted in a double peak, leading to mismatch with the triangular template and a below-threshold correlation. Second, the correlation of the Cr II 286.26 nm line exceeded the threshold, nevertheless, a slight shift of the line caused the assumed (non-shifted) center to fall below the S/N threshold. Thus, the above-threshold condition became false and the line undetected. Third, the lines Cr II 520.60 nm and Cr II 520.84 nm were intense and exceeded the threshold, but a shift of the correlated regions resulted in misalignment and low correlation.

These observations clearly demonstrate the limitations of the current approach. Although the assumption of systematic shift allows for fast allocation of the features, it fails to account for factors contributing to the shifts of individual lines, such as the Stark shift resulting from the presence of electric fields. This consideration is particularly important in electron-rich plasmas, like those generated from steel. Therefore, these limitations should be acknowledged and addressed in future extensions of the tool.

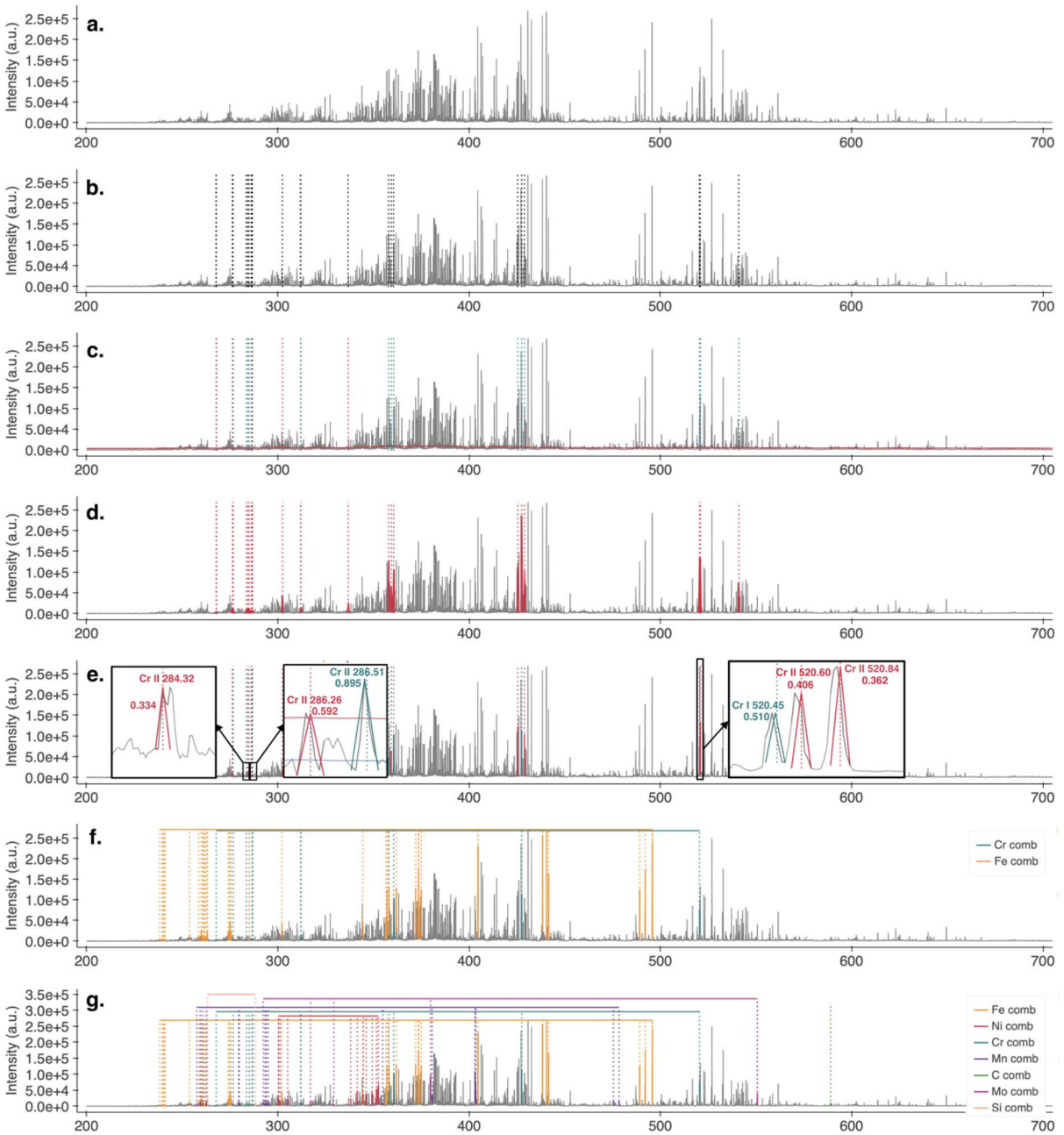

Fig. 4 Comb pipeline of low alloyed steel (SUS1R), laser energy: 75 mJ, gate delay: 4000 ns; (a) LIBS spectrum; (b) line allocation: theoretical lines of Cr; (c) threshold estimation: above-threshold lines of Cr; (d) template matching: default templates of Cr (shift 0.00 nm, width 1.00 nm, correlation active lines: 0.54); (e) template matching: optimized templates of Ba (shift 0.00 nm, width 0.10 nm, correlation active lines: 0.82); (f) interference analysis: combs of Cr and Fe; (g) feature visualization: elemental fingerprints of the 7 most prominent elements.

By listing possible interference, Fe emerged as a common alternative. Again, the interactive visualization of the corresponding fingerprints (Fig. 4f) provided a deep understanding of the possible overlaps.

The Fig. 4g shows the features of elements listed in Table 2. Given that the current version of the algorithm is highly prone to producing many false positives with complex spectra, this method of defining the elements to visualize is preferred until a more advanced approach, using the NIST database and automated filtering of the most likely lines, is implemented.

3.2 HSI of human tooth (single-channel Czerny–Turner): case of hyperspectral image

Having developed the algorithm, we were interested in its performance in real-life scenarios, particularly in its ability to generalize to different spectral types. Acquired with a single-channel Czerny–Turner setup, and relevant to the real-life applications, the hyperspectral image (HSI) of a human tooth provided a perfect opportunity for such a study.

Fig. 5a and b depict a longitudinal section of an extracted human molar in a microscopic and a hyperspectral image,

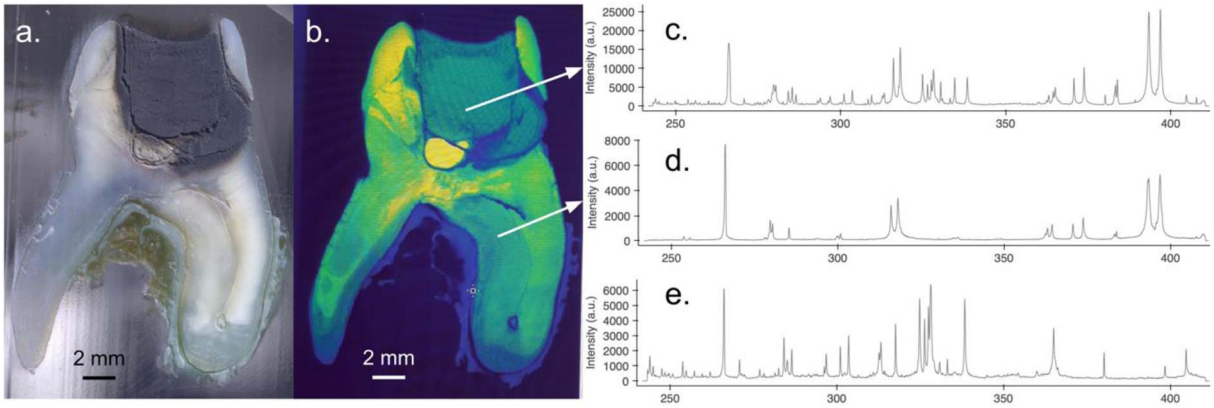

Fig. 5 Overview of the human tooth dataset: (a) microscopic image and (b) hyperspectral image of analyzed human tooth; (c) max acquired spectra; (d) spectrum of dental tissue; (e) spectrum of amalgam filling.

respectively. Both images show a visible contrast in the tooth crown section due to the presence of an amalgam filling. While the majority of the image represents dental matrix comprising biogenic elements such as Ca, Mg, P, Sr, and C, resulting in simple spectra (Fig. 5d), the amalgam filling contains transition elements, resulting in a significant increase in spectral lines within the observed spectral range (Fig. 5c).

3.2.1 Tooth filling. Compared to the Echelle spectra of borosilicate glass and low-alloyed steel, the spectrum of the human tooth comprised only a single channel, resulting in a limited spectral range for the analysis. As depicted in Fig. 6a (interactive version available at libsfeatex_demo_tooth (**https://colab.research.google.com/drive/1jw7uuW3CEQatMu53zh0gakPeZ2rJYnBN**)[33]), the spectrum was fairly simple, exhibiting low background emission and a limited number of lines. However, unlike the samples of Sections 3.1 Standard reference materials, the qualitative and quantitative information was not known *a priori* and had to be assumed.

Especially when the contents of the sample are not known, defining an element present in the sample can be problematic. Nevertheless, in most real-life cases, analysts already have an idea which element might be present, and even if not, the plots of theoretical lines allow for a good indication of which elements might be present and provide a reliable estimate of the shift. Given that the spectrum originated from a tooth filling, it seemed reasonable to assume the presence of Sn.

As illustrated in Fig. 6b, the theoretical lines of Sn aligned with a large fraction of the emission lines present in the spectrum, strongly supporting this assumption. The presence of the theoretical Sn lines was assessed by employing an S/N threshold. In this case, a window size of 8 nm and an upper 80 percentile of the signal-baseline deviation (accounting for the higher S/N ratio) was employed, which resulted in a flexible threshold allowing for good discrimination between the signal and the lines. As shown by Fig. 6c, all the Sn lines except one exceeded the threshold. Nevertheless, to further prove their presence, the regions were correlated with templates.

Again, the shifts and widths of the lines were unknown. Therefore, the templates were initiated at their theoretical positions (line shift of 0.00 nm, template width of 1.00 nm). As presented in Fig. 6d, the default width provided a relatively good estimate; nevertheless, the misalignment of the line and template centers hinted at a systematic shift. As the fingerprint of Sn seemed to account for the majority of spectral lines, it appeared to be a suitable reference element for the determination and adjustment of the shift.

After the refinement of the fingerprint positions, three of the Sn lines were assessed as inactive (Fig. 6e). Out of these, the Sn I 242.95 nm line was below the signal-to-noise threshold. In the case of Sn II 328.31 nm and Sn II 398.46 nm, an emission line in the region was present, but even after the fine allocation, the correlation was low, indicating that they might belong to some other element. Upon listing all other active lines in the region, the lines of Ag I 328.08 and Hg II 398.39 emerged as the most plausible alternatives. Again, through an interactive visualization of the corresponding fingerprints (here showing only Hg and Sn, Fig. 6f), the lines could be nicely resolved and clearly assigned.

For a comprehensive overview of the element-specific features stored in the spectrum, users can visualize selected fingerprints or top hits. As discussed previously, while top hits might provide an initial insight, the simplified assumptions of the current approach might result in artifacts. Thus, until the limitations are addressed, it is recommended to visualize the fingerprint of selected elements. This might be problematic in cases where the contents of the sample are unknown. Nevertheless, in such cases, the top hits might provide initial hints, and the users can further explore the contents of the sample by visualizing fingerprints of various elements. Additionally, in real-life scenarios, *a priori* information about the sample is typically available. For instance, in this case, the spectrum originates from a tooth filling. Thus, elements comprised in amalgam (Ag, Sn, Cu, Hg, and Zn) can be assumed and visualized. As an interactive overview of the respective fingerprints shows (Fig. 6 g), all the elements were detected, each providing multiple lines suitable for the subsequent analysis.

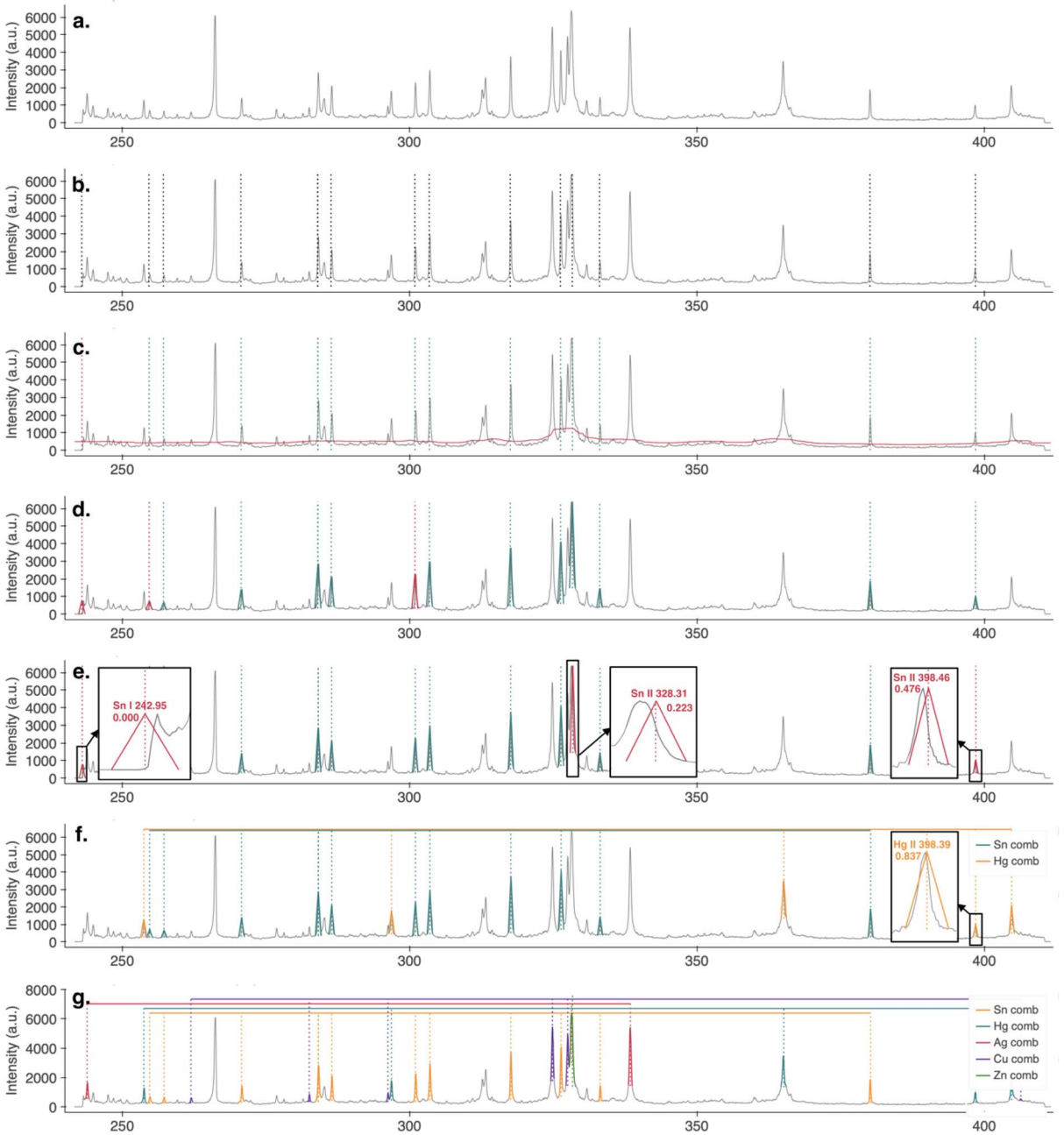

Fig. 6 Comb pipeline of human tooth filling: (a) LIBS spectrum; (b) line allocation: theoretical lines of Sn; (c) threshold estimation: above-threshold lines of Sn; (d) template matching: default templates of Sn (shift 0.00 nm, width 1.00 nm, correlation active lines: 0.61); (e) template matching: optimized templates of Sn (shift 0.08 nm, width 0.93 nm, correlation active lines: 0.84); (f) interference analysis: combs of Sn and Hg; (g) feature visualization: elemental fingerprints of Sn, Hg, Ag, Cu and Zn.

4 Conclusion

In this work, we introduced an intuitive tool for the allocation and visualization of element-specific features in LIBS spectra. Developed with the goal of universal applicability, the tool features only two basic parameters requiring little to no tuning: window size, which regulates the fit of the decision threshold, and the upper percentile from baseline deviation, which regulates the horizontal positioning of the threshold and thereby the sensitivity of the detection. While a smaller window size allows for more dynamic threshold adjustment, a lower percentile increases sensitivity but unavoidably raises the number of false positives.

The goal of universal applicability required significant simplifications on the development side. Consequently, the current version of the algorithm works with a limited database of lines resulting in incomplete coverage. This results in current limitations (increased number of false positives) which are planned to be addressed by employing a NIST database and

automated filtering of feasible lines based on plasma conditions in the future.

The correlation approach provides multiple advantages. Compared to a simple intensity-based approach, correlation is intensity independent. Thus, the combination of the correlation and a S/N-based detection threshold ensures the allocation of trace as well as major constituents of the sample. Additionally, providing information about the alignment of a theoretical with the allocated peak, the algorithm provides a valuable insight into the possible shift and broadening of the emission line, leaving the analyst with more information about the constituents of the sample.

Nevertheless, the shift and broadening do affect the line detection. In its current version, the algorithm automatically accounts for the uniform line shift (*e.g.* due to instrumental drift) and element-specific line broadening (*e.g.* due to Doppler broadening). The line-specific shift (*e.g.* Stark shift) and broadening (*e.g.* collisional broadening) are more complex and thus not accounted for, which might result in current detection inaccuracies, especially in the case of complex sample matrices.

The developed pipeline was successfully demonstrated on Echelle spectra of two standard reference materials, borosilicate glass (NIST1411) and low-alloy steel (SUS1R), showcasing its versatility across varying complexities. Furthermore, we demonstrated the tool's transferability and real-life applicability by applying it to a single-channel Czerny–Turner spectrum of an amalgam filling extracted from a hyperspectral image of a human tooth. While the tool performed well with the NIST spectra, capturing the relevant information, it required a semi-supervised approach for more complex spectra like SUS1R and the unknown filling spectrum. Nevertheless, even in this form, the tool proved to provide greatly valuable insights into the data, highlighting the information stored inside.

Data availability

The data analysis scripts of this article are available in the interactive notebooks libsfeatex_demo_NIST141, libsfeatex_demo_SUS1R and libsfeatex_demo_tooth available at **https://colab.research.google.com/drive/1qmlSMMNvt5_ZczR6bYlUr5KvTUiZVaQV#scrollTo=WPcZIwRddQYB**, **https://colab.research.google.com/drive/1G-UAWBh-ZBpL-Ztmyxf0Y6lddqsXRIzx#scrollTo=2vfxxwsGY4KS**, **https://colab.research.google.com/drive/1jw7uuW3CEQatMu53zh0gakPeZ2rJYnBN#scrollTo=hDyhL3iy7UfI**. The database of emission lines is available at **https://zenodo.org/records/13762624**. All of the links are properly stated and referenced in the article.

Conflicts of interest

There are no conflicts to declare.

Acknowledgements

ZG gratefully acknowledges the KUWI Grant of TU Wien. EK and AF acknowledge the support of Aktion Austria-Czech Republic. AF further acknowledges the support of Brno University of Technology project no. CEITEC VUT/FSI-J-24-8596. PP acknowledges the support of Czech Science Foundation (23-05186K) and JK acknowledges the support through the specific research grant from the Faculty of Mechanical Engineering, Brno University of Technology (FSI-S-23-8389).

References

1 A. Limbeck, L. Brunnbauer, H. Lohninger, P. Pořízka, P. Modlitbová, J. Kaiser, P. Janovszky, A. Kéri and G. Galbács, *Anal. Chim. Acta*, 2021, **1147**, 72–98.
2 K. Kiss, A. Šindelářová, L. Krbal, V. Stejskal, K. Mrázová, J. Vrábel, M. Kaška, P. Modlitbová, P. Pořízka and J. Kaiser, *J. Anal. At. Spectrom.*, 2021, **36**, 909–916.
3 B. Busser, S. Moncayo, J.-L. Coll, L. Sancey and V. Motto-Ros, *Coord. Chem. Rev.*, 2018, **358**, 70–79.
4 H. Kopřivová, K. Kiss, L. Krbal, V. Stejskal, J. Buday, P. Pořízka, M. Kaška, A. Ryška and J. Kaiser, *Anal. Chim. Acta*, 2024, **1310**, 342663.
5 C. Fabre, *Spectrochim. Acta, Part B*, 2020, **166**, 105799.
6 C. Alvarez-Llamas, A. Tercier, C. Ballouard, C. Fabre, S. Hermelin, J. Margueritat, L. Duponchel, C. Dujardin and V. Motto-Ros, *J. Anal. At. Spectrom.*, 2024, **39**, 1077–1086.
7 C. Fabre, L. Marulier, B. Monfaredi, V. Motto-Ros, B. Bousquet, A. Eglinger and A. Tarantola, *Spectrochim. Acta, Part B*, 2024, **216**, 106954.
8 L. Brunnbauer, S. Larisegger, H. Lohninger, M. Nelhiebel and A. Limbeck, *Talanta*, 2020, **209**, 120572.
9 T. Brennecke, L. Čechová, K. Horáková, L. Šimoníková, J. Buday, D. Prochazka, P. Modlitbová, K. Novotný, A. W. Miziolek, P. Pořízka and J. Kaiser, *Spectrochim. Acta, Part B*, 2023, **205**, 106684.
10 P. Modlitbová, S. Střítežská, A. Hlaváček, D. Prochazka, P. Pořízka and J. Kaiser, *Ecotoxicol. Environ. Saf.*, 2021, **214**, 112113.
11 R. C. Wiens, J. Becker, K. Benzerara, S. Bernard, B. Bousquet, K. Boyd, M. Caffrey, J. Carlson, K. Castro, J. Celis, B. Chide, E. Cloutis, E. C. Cordoba, D. Delapp, M. Deleuze, M. Dirmyer, C. Donny, G. Dromart, M. George Duran, M. Egan, J. Ervin, C. Fabre, A. Fau, O. Forni, T. Fouchet, D. Gasway, I. Gontijo, J. Grotzinger, X. Jacob, S. Jacquinod, J. R. Johnson, R. A. Klisiewicz, J. Lake, N. Lanza, J. Laserna, J. Lasue, S. Le Mouélic, C. Legett, R. Leveille, E. Lewin, G. Lopez-Reyes, R. Lorenz, E. Lorigny, S. P. Love, B. Lucero, J. M. Madariaga, M. Madsen, S. Madsen, N. Mangold, J. A. Manrique, J. P. Martinez, J. Martinez-Frias, K. P. McCabe, T. H. McConnochie, J. M. McGlown, S. M. McLennan, N. Melikechi, P.-Y. Meslin, J. M. Michel, D. Mimoun, A. Misra, G. Montagnac, F. Montmessin, V. Mousset, N. Murdoch, H. Newsom, L. A. Ott, Z. R. Ousnamer, L. Pares, C. Glen Peterson, P. Pilleri, P. Pinet, G. Pont, F. Poulet, C. Provost, W. Rapin, J.-M. Reess, A. H. Regan, A. L. Reyes-Newell, P. J. Romano, C. Royer, F. Rull, B. Sandoval, V. Sautter, M. J. Schoppers, S. Schröder, D. Seitz, T. Shepherd, P. Sobron, B. Dubois, V. Sridhar, M. J. Toplis, I. Torre-Fdez, I. A. Trettel,

M. Underwood, A. Valdez, D. Venhaus and P. Willis, *Space Sci. Rev.*, 2020, **217**, 4.
12 P. Bernardi, L. Parès, R. Newell, T. Nelson, O. Gasnault, J.-M. Réess, V. Schridar, I. Contijo, A. Reyes-Newell, G. E. Peterson, C. L. Iv, B. Dubois and S. H. Robinson, in *International Conference on Space Optics — ICSO 2020*, SPIE, 2021, vol. 11852, pp. 609–627.
13 H. Saeidfirozeh, P. Kubelík, V. Laitl, A. Křivková, J. Vrábel, K. Rammelkamp, S. Schröder, I. B. Gornushkin, E. Képeš, J. Žabka, M. Ferus, P. Pořízka and J. Kaiser, *TrAC, Trends Anal. Chem.*, 2024, **181**, 117991.
14 G. Amato, G. Cristoforetti, S. Legnaioli, G. Lorenzetti, V. Palleschi, F. Sorrentino and E. Tognoni, *Spectrochim. Acta, Part B*, 2010, **65**, 664–670.
15 J. J. Hatch, T. R. McJunkin, C. Hanson and J. R. Scott, *Appl. Opt.*, 2012, **51**, B155–B164.
16 I. Rosas-Román, M. A. Meneses-Nava, O. Barbosa-García and J. L. Maldonado, *Appl. Spectrosc.*, 2017, **71**, 627–633.
17 T. A. Labutin, S. M. Zaytsev and A. M. Popov, *Anal. Chem.*, 2013, **85**, 1985–1990.
18 V. Palleschi, *Chemometrics and Numerical Methods in LIBS*, Wiley, 2022.
19 V. Palleschi, *Laser Part. Beams*, 2023, **2023**, e2502152.
20 E. Képeš, J. Vrábel, T. Brázdil, P. Holub, P. Pořízka and J. Kaiser, *Talanta*, 2024, **266**, 124946.
21 National Institute of Standards and Technology (NIST), NIST Atomic Spectra Database, **https://physics.nist.gov/asd**, accessed June 11, 2024.
22 Bundesanstalt für Materialforschung und prüfung (BAM), Standard Reference Material SUS1R Low Alloyed Steel, **https://webshop.bam.de/media/wysiwyg/Kategorien/Referenzmaterialien/Eisen_Stahl/Spektrometer_Einstellprobe/Zertifikate/sus_1rde.pdf**, accessed June 11, 2024.
23 D. Prochazka, P. Pořízka, J. Hruška, K. Novotný, A. Hrdlička and J. Kaiser, *J. Anal. At. Spectrom.*, 2022, **37**, 603–612.
24 Atomic Spectra Database, **https://www.nist.gov/pml/atomic-spectra-database**, accessed June 4, 2024.
25 H. Lohninger and Gajarska, *Zenodo*, 2024, file gajarska_libs_db_20240916.txt, **https://zenodo.org/records/13762624**.
26 E. Képeš, P. Pořízka, J. Klus, P. Modlitbová and J. Kaiser, *J. Anal. At. Spectrom.*, 2018, **33**, 2107–2115.
27 D. A. Cremers and J. Radziemski, *Handbook of Laser-Induced Breakdown Spectroscopy*, 2013.
28 D. W. Hahn and N. Omenetto, *Appl. Spectrosc.*, 2010, **64**, 335A–336A.
29 D. W. Hahn and N. Omenetto, *Appl. Spectrosc.*, 2012, **66**, 347–419.
30 National Institute of Standards and Technology, Standard Reference Material 1411 Soft Borosilicate Glass, **https://tsapps.nist.gov/srmext/certificates/1411.pdf**, accessed June 11, 2024.
31 Z. Gajarska, libsfeatex_demo_NIST1411, **https://colab.research.google.com/drive/1qmlSMMNvt5_ZczR6bYlUr5KvTUiZVaQV#scrollTo=WPcZIwRddQYB**, accessed June 11, 2024.
32 Z. Gajarska, libsfeatex_demo_SUS1R, **https://colab.research.google.com/drive/1G-UAWBh-ZBpL-Ztmyxf0Y6ldddqsXRIzx#scrollTo=2vfxxwsGY4KS**, accessed June 11, 2024.
33 Z. Gajarska, libsfeatex_demo_tooth, **https://colab.research.google.com/drive/1jw7uuW3CEQatMu53zh0gakPeZ2rJYnBN#scrollTo=hDyhL3iy7UfI**, accessed June 13, 2024.